Catalysis Today 413-415 (2023) 113992

Contents lists available at ScienceDirect

Catalysis Today

journal homepage: www.elsevier.com/locate/cattod

Preparation, characterization and testing of a bulky non-supported photocatalyst for water pollution abatement

S.D. Aguilar [a,b,1], D.R. Ramos [a,*,1], J.A. Santaballa [a], M. Canle [a,*]

[a] React! Group, Department of Chemistry, CICA & Faculty of Sciences, Universidade da Coruña, Campus da Zapateira s/n, E-15071 A Coruña, Spain
[b] Department of Chemistry and Exact Sciences, Universidad Técnica Particular de Loja, 11 01 608 Loja, Ecuador

ARTICLE INFO

Keywords:
Photocatalyst
Semiconductor
Clay
Pellets
Photodegradation
Water treatment

ABSTRACT

An innovative bulky photocatalyst for water decontamination has been developed. The semiconductor (TiO_2) is homogeneously distributed in an aggregating material through the whole piece. This design prevents the activity reduction usually observed in supported catalysts due to the loss of the photoactive layer, and facilitates its recovery for an easy reuse, which is a recurrent problem dealing with nanoparticles. The photocatalyst combines the excellent properties of TiO_2 with those of a natural clay, which serves as binder, slows down the phase transition of anatase to rutile upon calcination, and has a synergetic function. The photocatalyst has been prepared in the form of small pellets with an Ecuadorian clay and TiO_2 in the commercial form of P25 by evenly dry mixing, forming a paste with water, and subsequent extrusion, drying and calcination at 600 °C. The photodegradation of phenol, as a model pollutant, has been achieved by using this aggregate material in a flow reactor with artificial UVA-Vis radiation, and reused without any significant loss of activity. The photocatalyst showed an optimum activity at a 40% clay / 60% P25 ratio, while higher calcination temperatures had a negative effect on its performance.

1. Introduction

The increasing occurrence of emergent contaminants and persistent organic pollutants (POPs) in the environment is an important concern worldwide and it also results in the quality degradation of the water supplies for human consumption [1,2]. Traditional water treatment plants, comprising physical, chemical and biological processes, consume large amounts of time, chemicals and energy, but cannot always remove these contaminants completely [3]. Many POPs have been detected in the effluents of treatment plants, and may accumulate in soils and also get transferred to the trophic chain [4], posing a risk to human health and the environment [5–8].

Advanced oxidation processes (AOPs) allow the removal of a broad range of organic compounds from water and wastewater through reactions with hydroxyl radicals ($HO^{\bullet}$) [9,10]. These chemical oxidations can be performed with the aid of primary oxidants (*e.g.*, O_3, H_2O_2, O_2, *etc.*), an energy supply (*e.g.*, UV irradiation, electricity), or a catalyst (*e.g.*, Fenton reagent, photocatalyst). Among them, heterogeneous photocatalysis has been pointed as the most promising technique for the degradation of these persistent compounds or their transformation to other biodegradable species [11]. Besides, sunlight-driven photocatalysis does not use any consumable reagent and it barely needs further energy, so it is probably the greenest and most economic AOP. A wider use of this technique has been mostly hampered by two factors: recoverability of the catalyst and reactor design [12].

Small size particulated photocatalysts (in the form of micro- or nanoparticles) are used in suspension, making it necessary to separate these fine particles from water after use by filtration or settling. This separation prevents an effective subsequent recovery and reuse of the catalyst [13–15]. Besides, this complex process could lead to the emission of environmentally toxic nanoparticles in the effluent [16,17]. Many techniques have been proposed for the immobilisation of the photocatalyst on solid supports to eliminate this problem [18,19]. However, supported catalysts also have some disadvantages, as compared to particulate photocatalysts, namely lower efficiency, higher preparation costs and a gradual loss of activity due to the detachment of the catalytic film [20–24].

Among many others materials, clays have some properties which make them appropriate for supporting photocatalysts: they are abundant, low-cost and environmentally friendly materials, with high

* Corresponding authors.
E-mail addresses: daniel.rramos@udc.es (D.R. Ramos), moises.canle@udc.es (M. Canle).
[1] First two authors contributed equally to this work

https://doi.org/10.1016/j.cattod.2022.12.023
Received 5 August 2022; Received in revised form 17 December 2022; Accepted 28 December 2022
Available online 29 December 2022

thermal, chemical and mechanical stability [25,26]. Furthermore, clays provide high surface area, porosity, and a large volume of surface active sites resulting in TiO_2/clay nanocomposites more photoactive than pure TiO_2 [27]. Thus, despite research has been abundant on clay-based photocatalytic nanocomposites, there is a lack of studies on making of and photodegradation mediated by TiO_2/clay macrocomposites.

We present a novel photocatalyst (patent application: PCT/ES2021/070940), where the TiO_2 semiconductor is not simply immobilized at the surface of a supporting material, but homogeneously mixed with an aggregating material to form a bulky composite without any catalytic film that can be peeled off, which can be directly employed. Such an economic, easy to use and recover photocatalyst that can be produced in sufficient amount and with adequate size and density, will permit a more extensive use of photocatalysis for water and wastewater treatment. In fact, a successful trial at a larger scale with this photocatalyst (but with a different clay) has already been published [28].

2. Experimental

2.1. Materials

A natural clay (P_1M_2), with origin from the Miocene sedimentary basin in Loja (Ecuador), was dried (90 °C), milled and sieved (mesh 250 μm), and used without any further purification. Degussa Aeroxide P25 TiO_2, referred to as TiO_2 hereafter, was the photocatalyst selected for the preparation of the composites. PanReac AppliChem phenol (98.5%) was selected as pollutant model. Organic matter-free bidistilled water was used for all solutions and processes but for HPLC mobile phase, where Milli-Q ultrapure water and Baker gradient HPLC-grade acetonitrile were employed. PanReac AppliChem hydrochloric acid (37%) and sodium hydroxide (>98%) were used for pH adjustment.

2.2. Preparation of photocatalytic composites

Dry clay and TiO_2 powders in the desired mass ratio (from 0% to 100% TiO_2 in 20% steps) were mixed thoroughly to yield a homogeneous mixture. Then, water was added dropwise while gently stirring until reaching the adequate plasticity to allow extrusion. This mixture was manually extruded with a 2 mm-inner diameter-tip syringe to produce elongated spaghetti-like rolls on a clean aluminium film, and they were dried at 90 °C for 12 h in an oven. These rolls were broken into smaller pellets (*ca.* 0.5 cm long on average, small enough to use *ca.* 1 g load with an easy handling size for recovering) and calcined at 600 °C (or other temperatures when indicated) for 3 h in porcelain capsules in a muffle furnace, using a 5 °C·min^{-1} heating ramp. Then, they were allowed to cool down slowly to room temperature inside the furnace. After rinsing with enough water to remove any powder or loose particles, they were dried again at 90 °C.

2.3. Characterization of the composites

The chemical semi-quantitative composition of clay and TiO_2 was determined by X-ray fluorescence (XRF) in a Bruker S4 Pioneer XRF spectrometer, while their particle size distribution was measured by laser light scattering in a Micromeritics Saturn DigiSizer II instrument. The identification of mineral crystalline phases of both initial materials and composites was performed by X-ray diffraction (XRD) in a Bruker D4 Endeavor X-ray diffractometer. The organic matter content of the clay was quantified as total organic carbon (TOC) and total nitrogen (TN) with a Skalar Formacs TOC/TN analyser, following catalytic combustion and oxidation of the material. The density of solid samples was obtained with a He pycnometer (Micromeritics Accupyc 1340). The surface of the pellets was examined by field emission scanning electron microscopy (FESEM), either taking electron micrographs or energy-dispersive X-ray spectroscopy (EDS) images, in a Jeol JSM-7200F device. The hardness of the aggregates was quantified by testing their resistance to fracture by compression with an Aliyiqi AMF-20 dynamometer. Specific surface area was obtained by N_2 adsorption using the BET isotherm in a Micromeritics TriStar II Plus analyser, and average pore size was also determined. Temperature-dependent changes were monitored by thermogravimetric analysis (TGA) under N_2 in a Netzsch STA 449 F3 Jupiter thermal analyser. The band gap was calculated by using Tauc plots [29], determining the Kubelka-Munk function [30] from diffuse reflectance measurements of the solid composites (shaped as flat tablets for this test) obtained in a UV-Visible spectrophotometer (Thermo Scientific Evolution 260 BIO) equipped with an integrating sphere.

2.4. Photodegradation experiments

Photocatalysis degradation experiments were performed in a flow reactor consisting of an 11.4 mm-internal diameter borosilicate tube situated horizontally, aligned with a Heraeus TQ 150 Z medium-pressure mercury-vapour lamp. The radiation was filtered out below 350 nm with a DURAN 50 glass jacket and thermostatted at 25 °C. The maximum emission line lies at $\lambda = 365$ nm, the irradiation on the pellets at this wavelength was measured with a Vilber Lourmat VLX-3W radiometer. This tube-lamp assembly was surrounded by a cylindrical aluminium reflector to maximize the efficiency, and the photocatalytic pellets (1 g) were allocated along 6 cm of this tube in a single layer, the same length as the lamp bulb, between two glass fibre stoppers (Scheme 1).

A 250 mL phenol solution (10 mg·L^{-1}), contained in a 25 °C thermostatted round flask, continuously stirred by bubbling, was circulated at 110 mL·min^{-1} with a peristaltic pump to the irradiated tube, where it slowly flowed on the pellets in a laminar regime (Reynolds number Re ≈ 230), with a retention hydraulic time of 3.34 s, for 3 h. Regularly 1 mL aliquots were taken for analysis. A photolysis test was also carried out without any photocatalyst, *ceteris paribus*. Also, Fenton experiments were performed in the dark at 25 °C, in a continuously stirred batch reactor: pristine clay (1.0 g·L^{-1}) and H_2O_2 (1.0 mmol·L^{-1}) were added to a 250 mL phenol solution (10 mg·L^{-1}) with pH adjusted to 2.5 (with HCl), 11.0 (with NaOH), or left unchanged (5.25).

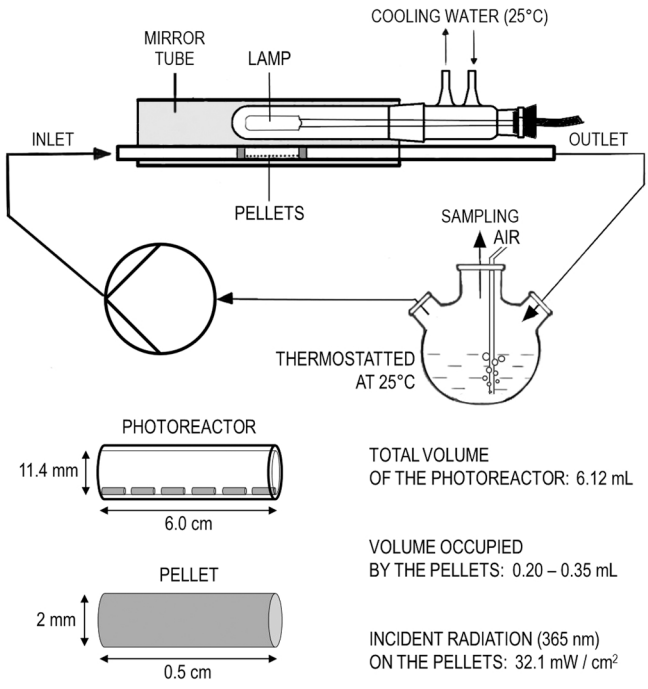

Scheme 1. Diagram of the flow photoreactor used in the study.

2.5. Analysis

Phenol analysis was performed by HPLC with a diode array UV-Vis instrument (Spectra System by Thermo Finnigan) and a reverse-phase C18 Hypersil ODS-2 column (150 × 4.6 mm, 5 μm particles). 1 mL·min^{-1} isocratic 75:25 H_2O/acetonitrile mobile phase was used and 50 μL samples were injected and monitored at 270 nm for 15 min runs. Full spectra were also taken for identity confirmation. A Shimadzu TOC 5000A analyzer was used to obtain the total organic carbon (TOC) values and so determine the degree of mineralization. The identification of the obtained photoproducts was performed by their spectra and retention time and compared to previous complete analysis [24].

3. Results and discussion

3.1. Characterization of the composites

P_1M_2 clay is mostly composed of SiO_2, Al_2O_3 and Fe_2O_3, adding up almost 90% of its total weight, plus other minor components (Table 1). Composition of the 100% clay pellets is similar, with some differences due to the calcination step. An unknown compound was present (loss on ignition accounts for *ca.* 11%), which could be either adsorbed on the surface or come from a component that was dissolved in the water used. BaO, P_2O_5, and Cl are missing in the pellets. In the presence of water, BaO converts into BaOH, which is extremely water soluble and can be withdrawn together with any soluble chlorine salts or oxides by rinsing. Also, P_2O_5 reacts with water to yield HPO_3, which can be evaporated during calcination (boiling point = 600 °C). Besides, other small concentration disparities arise from the common heterogeneity of a natural clay. The organic matter present in the clay is very low, TOC and TN only represent 15.5 and 0.727 mg/L, respectively, but they are lost during calcination. On the other hand, the FRX analysis of commercial TiO_2-P25 detected a high purity compound (99.8%) with some impurities identified as Cl and CuO.

According to the particle size analysis (Fig. S1 of the supplementary material), P_1M_2 displays a wide range of grain dimensions, where particles sized between 1.2 and 61.4 μm amount to 90% of total volume and show a mode value of 10.0 μm. TiO_2 particles show a smaller size, with 90% of the volume comprised between 0.85 and 13.7 μm, and the mode is 4.2 μm. A low BET specific surface area (32.7 m^2·g^{-1}) develops from the coarse particulate clay, whereas TiO_2 has a higher surface area (50.9 m^2·g^{-1}). Both materials have pores of similar size, with average diameters around 66 Å, *i.e.* they are mesoporous materials, although the median pore widths are much smaller (*ca.* 7.7 Å), indicating that a few big pores increase the average value but most pores are small and would correspond to microporous materials. The TGA of the P_1M_2 clay yielded a total weight loss of 10.92% at 900 °C, where only 3.02% corresponds to water dried at 105 °C, and the most significant mass changes take place at 361.4 and 602.8 °C (Fig. S2). Subsequent loss is not consistent with thermolysis and vaporization of organic matter and other labile compounds, since they do not account for such an amount. Thus, the remaining percentage lost (7.90%) must be mainly assigned to crystallization water.

The formation and calcination of photocatalytic aggregates also influence other physical properties, summarized in Table 1. 100% clay pellets have almost twice the density of the raw powder, as the material undergoes a sintering process and gets more packed when fired; this results in an important reduction of its surface area. However, 100% TiO_2 pellets also reduce their surface with respect to starting TiO_2, but the density is barely affected. Less dense pellets with higher surface areas were obtained upon combination of these materials, probably because the structures are not as closely packed as in the pure materials, with both values increasing with TiO_2 percentage. Still, these composites have a specific weight high enough to remain static under a moderate water flow, forming a stationary phase at the bottom. While median pore width does not change significantly, larger average pores were obtained in the pellets with respect to starting powders, and this value is not much affected by composition. Therefore, aggregate materials also have a mesoporous surface, with widely dispersed pore sizes. These pellets show an irregular surface at the micro level (Fig. S3), where small TiO_2 particles are homogeneously mixed with the clay in some areas but also covering some bigger structures of the latter. Still, overall, silica and titania are evenly distributed through the composites surface according to their composition ratios (Figs. S4 and S5), although

Table 1
Chemical analysis (%) of starting raw materials and 100% clay pellets measured by XRF (obtained compounds in concentration higher than 0.01% in weight percentage) and physical properties measured for starting raw materials and clay/TiO_2 pellets: density (g·mL^{-1}), resistance to fracture by compression strength (N), BET specific surface area (m^2·g^{-1}), and average and median pore width (Å).

	Composition									
P_1M_2 clay	SiO_2	Al_2O_3	Fe_2O_3	SO_3	K_2O	MgO	CaO	Na_2O	TiO_2	P_2O_5
	67.5	15.6	6.4	3.1	2.8	1.9	0.96	0.72	0.48	0.15
	Cl	BaO	MnO	ZrO_2	SrO	ZnO	CuO	Rb_2O		
	0.12	0.083	0.031	0.016	0.014	0.013	0.013	0.012		
P_1M_2 pellets	SiO_2	Al_2O_3	Fe_2O_3	SO_3	K_2O	MgO	Na_2O	CaO	TiO_2	MnO
	65.5	16.3	5.6	3.9	2.8	2.5	1.2	1.1	0.60	0.026
	ZrO_2	SrO	CuO	ZnO	Rb_2O					
	0.022	0.019	0.018	0.017	0.016					
TiO_2-P25	TiO_2	Cl	CuO							
	99.8	0.12	0.017							

	Density	Compression strength	BET specific surface area	Pore width	
				Average	Median
P_1M_2 clay	2.82	-	32.7	65.9	7.68
TiO_2-P25	4.38	-	50.9	65.7	7.71
Pellets 600 °C					
0% TiO_2	4.96	14.8	14.9	85.2	7.72
20% TiO_2	2.88	8.7	27.6	94.0	7.69
40% TiO_2	3.09	7.9	38.2	89.6	7.72
60% TiO_2	3.30	5.9	42.5	90.3	7.66
80% TiO_2	3.60	3.8	43.1	84.6	7.73
100% TiO_2	4.24	6.0	33.3	94.3	7.74
Pellets 60% TiO_2					
500 °C	3.31	3.6	40.1	91.5	7.69
700 °C	3.35	6.6	28.6	84.0	7.72

the presence of particles of quite different composition is randomly observed in some areas (Fig. S6), indicating the natural heterogeneity of the clay. This arrangement must be responsible of the increase in BET for the composite materials with respect to pure clay or TiO_2 pellets.

According to XRD measurements, some SiO_2 content in P_1M_2 (Fig. 1A) is crystallized as quartz (2θ = 20.8° and 26.6°). Also, SiO_2, Al_2O_3 and Fe_2O_3, among others, may form non-crystalline phases, detected as background signal. Besides, any crystalline phase of minor TiO_2 content could not be observed. The diffractogram does not present any relevant differences upon calcination (Fig. 1B).

TiO_2-P25 (Fig. 1C) is mostly in the form of anatase (76%, 2θ = 25.3°), while rutile is found at a lower concentration (24%, 2θ = 27.5°). This is consistent with some anatase/rutile ratios published in the literature [31]. However, TiO_2 calcination resulted in some changes in XRD patterns. Pure TiO_2-pellets diffractogram (Fig. 1D) indicates a severe anatase to rutile transformation, resulting in a similar final concentration of both phases. However, some clay content (20%) in the pellets (Fig. 1E) prevents this phase transition. Thermal anatase to rutile phase transformation takes place from ~600 °C at normal pressure, but it is affected by the presence of impurities and dopants, these species having either positive or negative effect [32]. The overall effect of the composition of P_1M_2 clay represents an important inhibition of this transformation.

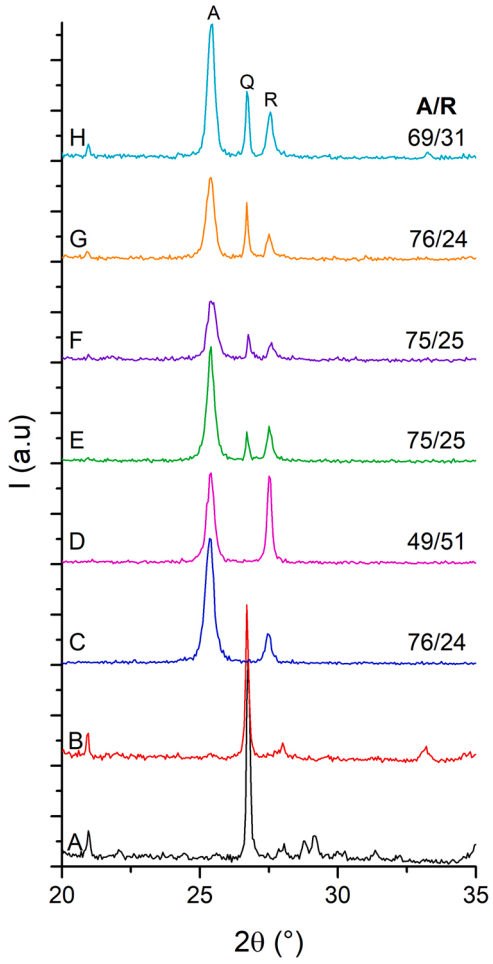

Fig. 1. XRD patterns in arbitrary units in the range 2θ = 20–35° of (A) untreated P_1M_2 clay, (B) pellets of 100% clay calcined at 600 °C, (C) untreated TiO_2-P25, pellets of (D) 100% and (E) 80% TiO_2 calcined at 600 °C, and 60% TiO_2 pellets calcined at (F) 500, (G) 600, and (H) 700 °C. The position of the main anatase (A), rutile (R) and quartz (Q) peaks are shown in diffractogram H. The anatase/rutile ratio obtained in each case is displayed. Full diffractograms are collected in Fig. S7.

Pellets containing 40% of the clay and calcined at either 500 or 600 °C also show an unmodified ratio between phases (Fig. 1F, G), and the temperature does not affect other physical properties (Table 1). However, relevant changes are observed in the 700 °C pellets: some phase shift (Fig. 1H) has been determined in this case, accompanied by a significant reduction of the surface area and some density increase.

Crystallite sizes were measured for the different materials used. The results show the clay has a main α-quartz phase with crystallites of *ca.* 55 nm. When processing the clay to obtain pellets, this size increases slightly to ~63 nm. All composite pellets show a main anatase peak with crystallite sizes ranging 21–27 nm. Analyzed in the same way, a sample of P25 showed anatase and rutile phases with crystallites of 23 and 36 nm size, respectively.

Another important parameter for the photocatalyst easiness of use and reuse is its resistance to fracture. The hardness of these aggregates strongly depends on their composition and calcination temperature (Table 1). Thus, the higher the clay content, the harder the resulting material. Besides, pellets obtained with higher temperatures resist stronger compressions. Finally, an essential parameter to evaluate the catalytic activity of a semiconductor is the band gap. This energy barrier has been measured for 60% and 80% TiO_2 composites (Fig. S8). Mean values are 3.16 (60%) and 3.12 (80%) eV, which correspond to 393 and 397 nm, respectively.

3.2. Phenol photodegradation

The activity of these photocatalytic pellets has been tested by monitoring phenol photodegradation in a simple flow reactor with a UVA-Vis lamp emitting mainly at 365 nm (Fig. S9), corresponding to an irradiation of 32.1 mW/cm^2 at this wavelength at the pellets distance. The photolytic effect of only UVA-Vis irradiation was tested in the absence of photocatalyst (Fig. 2A), reducing only ~11% phenol in 3 h. The first-order rate constants for all degradation experiments are collected in Table 2. Due to the presence of a low percentage (6.4%) of Fe_2O_3 in the clay, the possibility of Fenton-type processes being involved must be considered. Hence, adsorption and Fenton processes were studied with the clay in the dark at natural pH as well as under acid and basic pH conditions (Fig. S10), while the photo-Fenton reaction was considered with 100% clay pellets under UVA-Vis radiation (Fig. 2A). Unlike other clays [33], neither degradation nor adsorption were observed in any case, but a negligible increase in the rate constant with respect to photolysis (~10%) in the irradiated experiment (Table 2). Thus, no significant distortion from this effect is expected in the photocatalyzed degradation experiments.

The photocatalytic activity of the pellets, prepared with different clay and TiO_2 mass ratios, has been studied at 4 g·L^{-1} photocatalyst load, *i.e.*, 1 g of pellets in 250 mL phenol solution (Fig. 2A). The corresponding kinetic constants display a strong dependence on the composition. Pure clay pellets do not show any catalytic activity, and the rate constant obtained is compatible with that for the photolysis trial. On the other hand, 100% TiO_2 pellets have a relevant activity but lower than any other TiO_2-clay combination. This enhancement is mostly caused by the higher anatase/rutile ratio in the calcined pellets containing P_1M_2 clay, and to the greater surface area (in all cases but 20% TiO_2 composites) as compared to the pure TiO_2 material. 20% TiO_2 pellets show higher catalytic activity, despite having such a small quantity of the semiconductor. Then, the composites with 40–80% TiO_2 behave alike, with a similar capacity for degrading phenol, slightly higher for the 60% TiO_2 pellets. The faster rates observed for these three materials can be easily explained in terms of their anatase/rutile ratio, TiO_2 content and surface area. These two properties also support the higher kinetic constant obtained for the 60% TiO_2 type with respect to 40% TiO_2, but the reduced activity of the pellets with 80% TiO_2 cannot be justified with the current data. Furthermore, this material shows a slightly lower band gap than 60% aggregates, although 365 nm photons should be equally absorbed and electrons promoted to the conduction band in both cases.

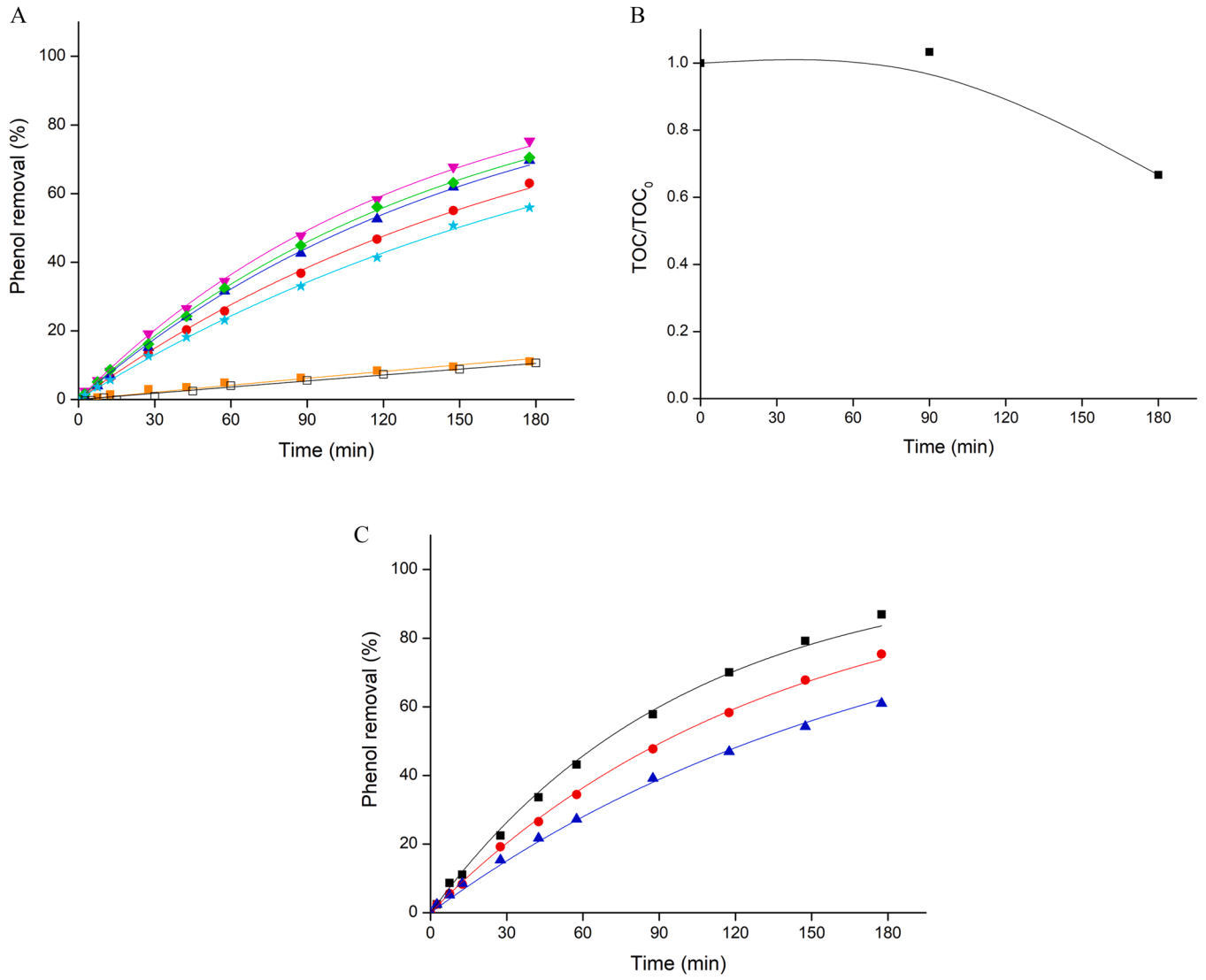

Fig. 2. Phenol removal in a flow reactor with a UVA-Vis lamp by (A) photolysis (□) and photocatalysis with photoactive composites of clay/TiO_2 calcined at 600 °C: [TiO_2] = 0% (■), 20% (●), 40% (▲), 60% (▼), 80% (♦), and 100% (★); (B) phenol mineralization with photocatalytic pellets of 40% clay and 60% TiO_2 calcined at 600 °C; and (C) phenol removal by photocatalysis with the same photocatalysts, calcined at 500 (■), 600 (●), and 700 °C (▲).

Table 2
First-order rate constants obtained for phenol removal in the different tests shown in Fig. 2. Results for reuse of these pellets are shown into parentheses.

Calcination T (°C)	Photocatalyst composition (% TiO_2)	$k \times 10^6$ (s^{-1})	
-	-	10.3 ± 0.3	
500	60	170 ± 3	
600	0	11.9 ± 0.4	
600	20	89.8 ± 0.8	
600	40	108.0 ± 1.1	(105.7 ± 1.1)
600	60	125.7 ± 1.2	(102.5 ± 0.9)
600	80	113.8 ± 0.8	(123 ± 2)
600	100	77.5 ± 0.6	
700	60	91.2 ± 1.4	

The observed effect can be attributed to a lower quantum efficiency for the process in this case, perhaps connected to e^--h^+ recombination efficiency. The use of a higher amount of clay has two further important advantages: it provides an improved mechanical stability and reduces the cost of the final product, as it is quite inexpensive, with a price that could even less than 1% of that of TiO_2-P25. The photodegradation of phenol with the best photocatalyst (60% TiO_2) corresponds to a 33% mineralization at 3 h (Fig. 2B), while the final products obtained are collected in Fig. S11.

Concerning the stability of these composites, the three materials with better activity have been collected after the first use, rinsed with water and employed again in a second run. Considering that the layout of the pellets in the reactor tube must be different, kinetic results are very similar (Table 2), although 80% TiO_2 pellets yielded the fastest degradation. Recovering and reuse of these pellets is very simple due to their bulky nature. Besides, the bulk composition of this material is the same as at the surface. Thus, its mechanical strength, although important, is less relevant than in supported photocatalysts, since the abrasion of the surface or the breakage of the particles should not cause the loss of active area.

The photocatalytic activity has been also monitored with respect to calcination temperature (Fig. 2C). At 700 °C the performance of the pellets decreases, mostly due to the anatase to rutile phase transition and

the reduction of surface area. The improved activity of 500 °C composites can be explained in a way similar to that previously used for the 60% TiO_2 pellets. The resistance to fracture by compression strength has been here selected as the critical factor for choosing 600 °C pellets, since they allow better handling, recovery and reuse. However, calcination temperature must be chosen according to the projected use and working conditions.

4. Conclusions

An innovative photocatalytic composite material is presented, based on a composite of a natural clay with homogeneously mixed TiO_2-P25. This material, when extruded in the form of pellets, shows ideal properties for its implementation in small water treatment facilities. This easy-to-use, bulky and durable photocatalytic material shows good recoverability features, with a very low production cost and a satisfactory catalytic activity.

The presence of the clay inhibits the anatase to rutile phase transformation upon calcination. The clay also enhances the mechanical strength, density and surface area of the resulting material, while other doping and synergistic effects cannot be discarded. Phenol removal using this material (40:60 clay/TiO_2) reaches *ca.* 85% after 3 h of UVA-Vis irradiation, together with a 33% mineralization degree.

CRediT authorship contribution statement

S. D. Aguilar: Conceptualization, Methodology, Formal analysis, Investigation, Writing – original draft. **D. R. Ramos:** Conceptualization, Methodology, Formal analysis, Investigation, Writing – original draft, Writing – review & editing. **J. A. Santaballa:** Writing – review & editing, Supervision, Funding acquisition. **M. Canle:** Writing – review & editing, Supervision, Funding acquisition.

Declaration of Competing Interest

The authors declare the following financial interests/personal relationships which may be considered as potential competing interests: S. D. Aguilar has patent #PCT/ES2021/070940 pending to Universidade da Coruña & Universidad Técnica Particular de Loja. D. R. Ramos has patent #PCT/ES2021/070940 pending to Universidade da Coruña & Universidad Técnica Particular de Loja. J. A. Santaballa has patent #PCT/ES2021/070940 pending to Universidade da Coruña & Universidad Técnica Particular de Loja. M. Canle has patent #PCT/ES2021/070940 pending to Universidade da Coruña & Universidad Técnica Particular de Loja.

Data Availability

Data will be made available on request.

Acknowledgements

This research has received funds from the Spanish Ministerio de Ciencia e Innovación [project PID2021-127898OB-I00], and the regional government Xunta de Galicia [GPC project ED431B 2020/52], to finance a contract to DRR. Funding for open access charge: Universidade da Coruña/CISUG. DRR also acknowledges UDC for a *Margarita Salas* contract and SDA acknowledges UTPL for financial support for pursuing PhD studies at UDC.

Appendix A. Supporting information

Supplementary data associated with this article can be found in the online version at doi:10.1016/j.cattod.2022.12.023.

References

[1] J. Ge, Y. Zhang, Y.-J. Heo, S.-J. Park, Advanced design and synthesis of composite photocatalysts for the remediation of wastewater: a review, Catalysts 9 (2019) 122.
[2] N. Chaukura, G. Katengeza, W. Gwenzi, C.I. Mbiriri, T.T.I. Nkambule, M. Moyo, A. T. Kuvarega, Development and evaluation of a low-cost ceramic filter for the removal of methyl orange, hexavalent chromium, and *Escherichia coli* from water, Mater. Chem. Phys. 249 (2020), 122965.
[3] Y. Deng, C. Guo, H. Zhang, X. Yin, L. Chen, D. Wu, J. Xu, Occurrence and removal of illicit drugs in different wastewater treatment plants with different treatment techniques, Environ. Sci. Eur. 32 (2020) 28.
[4] Y. Chen, C. Wang, Z. Wang, Residues and source identification of persistent organic pollutants in farmland soils irrigated by effluents from biological treatment plants, Environ. Int. 31 (2005) 778–783.
[5] S.-H. Lee, J.-S. Ra, J.-W. Choi, B.-J. Yim, M.-S. Jung, S.-D. Kim, Human health risks associated with dietary exposure to persistent organic pollutants (POPs) in river water in Korea, Sci. Total Environ. 470–471 (2014) 1362–1369.
[6] V. Linares, G. Perelló, M. Nadal, J. Gómez-Catalán, J.M. Llobet, J.L. Domingo, Environmental versus dietary exposure to POPs and metals: a probabilistic assessment of human health risks, J. Environ. Monit. 12 (2010) 681–688.
[7] A. Pawełczyk, Assessment of health risk associated with persistent organic pollutants in water, Environ. Monit. Assess. 185 (2013) 497–508.
[8] O. Alharbi, A. Basheer, R. Khattab, P.I. Ali, Health and environmental effects of persistent organic pollutants, J. Mol. Liq. 263 (2018).
[9] A. Christensen, M.D. Gurol, T. Garoma, Treatment of persistent organic compounds by integrated advanced oxidation processes and sequential batch reactor, Water Res. 43 (2009) 3910–3921.
[10] M.J. Martín de Vidales, M. Millán, C. Sáez, P. Cañizares, M.A. Rodrigo, Irradiated-assisted electrochemical processes for the removal of persistent pollutants from real wastewater, Sep. Purif. Technol. 175 (2017) 428–434.
[11] A.R. Ribeiro, O.C. Nunes, M.F.R. Pereira, A.M.T. Silva, An overview on the advanced oxidation processes applied for the treatment of water pollutants defined in the recently launched Directive 2013/39/EU, Environ. Int. 75 (2015) 33–51.
[12] E.L. Cates, Photocatalytic water treatment: so where are we going with this? Environ. Sci. Technol. 51 (2017) 757–758.
[13] S. Kagaya, K. Shimizu, R. Arai, K. Hasegawa, Separation of titanium dioxide photocatalyst in its aqueous suspensions by coagulation with basic aluminium chloride, Water Res. 33 (1999) 1753–1755.
[14] A. Rachel, M. Subrahmanyam, P. Boule, Comparison of photocatalytic efficiencies of TiO_2 in suspended and immobilised form for the photocatalytic degradation of nitrobenzenesulfonic acids, Appl. Catal. B 37 (2002) 301–308.
[15] H.T. Wang, Y.Y. Ye, J. Qi, F.T. Li, Y.L. Tang, Removal of titanium dioxide nanoparticles by coagulation: effects of coagulants, typical ions, alkalinity and natural organic matters, Water Sci. Technol. 68 (2013) 1137–1143.
[16] V. Nogueira, I. Lopes, T. Rocha-Santos, F. Gonçalves, R. Pereira, Toxicity of solid residues resulting from wastewater treatment with nanomaterials, Aquat. Toxicol. 165 (2015) 172–178.
[17] L. Canesi, C. Ciacci, T. Balbi, Interactive effects of nanoparticles with other contaminants in aquatic organisms: Friend or foe? Mar. Environ. Res. 111 (2015) 128–134.
[18] M.H. Alhaji, K. Sanaullah, A. Khan, A. Hamza, A. Muhammad, M.S. Ishola, A.R. H. Rigit, S.A. Bhawani, Recent developments in immobilizing titanium dioxide on supports for degradation of organic pollutants in wastewater- A review, Int. J. Environ. Sci. Technol. 14 (2017) 2039–2052.
[19] M.A. Mohd Adnan, N. Muhd Julkapli, M.N.I. Amir, A. Maamor, Effect on different TiO_2 photocatalyst supports on photodecolorization of synthetic dyes: a review, Int. J. Environ. Sci. Technol. 16 (2019) 547–566.
[20] K.V.S. Rao, M. Subrahmanyam, P. Boule, Immobilized TiO_2 photocatalyst during long-term use: decrease of its activity, Appl. Catal. B 49 (2004) 239–249.
[21] J. Kumar, A. Bansal, A comparative study of immobilization techniques for photocatalytic degradation of Rhodamine B using nanoparticles of titanium dioxide, Water Air Soil Pollut. 224 (2013) 1452.
[22] I. Levchuk, C. Guillard, F. Dappozze, S. Parola, D. Leonard, M. Sillanpää, Photocatalytic activity of TiO_2 films immobilized on aluminum foam by atomic layer deposition technique, J. Photochem. Photobiol. A 328 (2016) 16–23.
[23] J.J. Rueda-Marquez, I. Levchuk, P. Fernández Ibañez, M. Sillanpää, A critical review on application of photocatalysis for toxicity reduction of real wastewaters, J. Clean. Prod. 258 (2020), 120694.
[24] D.R. Ramos, M. Iazykov, M.I. Fernandez, J.A. Santaballa, M. Canle, Mechanical stability is key for large-scale implementation of photocatalytic surface-attached film technologies in water treatment, Front. Chem. Eng. 3 (2021), 688498.
[25] J. Herney-Ramirez, M.A. Vicente, L.M. Madeira, Heterogeneous photo-Fenton oxidation with pillared clay-based catalysts for wastewater treatment: a review, Appl. Catal. B 98 (2010) 10–26.
[26] E.G. Garrido-Ramírez, B.K.G. Theng, M.L. Mora, Clays and oxide minerals as catalysts and nanocatalysts in Fenton-like reactions - a review, Appl. Clay Sci. 47 (2010) 182–192.
[27] A. Mishra, A. Mehta, S. Basu, Clay supported TiO_2 nanoparticles for photocatalytic degradation of environmental pollutants: a review, J. Environ. Chem. Eng. 6 (2018) 6088–6107.
[28] M. Sánchez, D.R. Ramos, M.I. Fernández, S. Aguilar, I. Ruiz, M. Canle, M. Soto, Removal of emerging pollutants by a 3-step system: Hybrid digester, vertical flow constructed wetland and photodegradation post-treatments, Sci. Total Environ. 842 (2022), 156750.

[29] P. Makuła, M. Pacia, W. Macyk, How to correctly determine the band gap energy of modified semiconductor photocatalysts based on UV–Vis spectra, J. Phys. Chem. Lett. 9 (2018) 6814–6817.
[30] R. López, R. Gómez, Band-gap energy estimation from diffuse reflectance measurements on sol-gel and commercial TiO_2: a comparative study, J. Sol. Gel Sci. Technol. 61 (2012) 1–7.
[31] B. Ohtani, O.O. Prieto-Mahaney, D. Li, R. Abe, What is Degussa (Evonik) P25? Crystalline composition analysis, reconstruction from isolated pure particles and photocatalytic activity test, J. Photochem. Photobiol. A 216 (2010) 179–182.
[32] D.A.H. Hanaor, C.C. Sorrell, Review of the anatase to rutile phase transformation, J. Mater. Sci. 46 (2011) 855–874.
[33] M. Djebbar, F. Djafri, M. Bouchekara, A. Djafri, Adsorption of phenol on natural clay, Appl. Water Sci. 2 (2012) 77–86.